Exploiting remote imagery in an embayed sandy beach for the validation of a runup model framework

Nico Valentini, Alessandra Saponieri, Alessandro Danisi, Luigi Pratola, Leonardo Damiani

Exploiting remote imagery in an embayed sandy beach for the validation of a runup modelling chain

Nico Valentini[a,b,*], Alessandra Saponieri[a], Alessandro Danisi[a], Luigi Pratola[a], Leonardo Damiani[a]

[a] *Department of Civil, Environmental, Building Engineering and Chemistry (DICATECh), Politecnico di Bari, Bari 70126, Italy*
[b] *BRGM, Occitanie-Pyrénées-Méditerranée (SGR/LRO), 1039 rue de Pinville, 34000 Montpellier, France*

Abstract

In the present paper, a numerical chain aimed at predicting wave-induced runup on an embayed sandy beach is validated by means of measurements derived from a video-monitoring station, recently installed in Southern Italy, during two storm events in 2016. The numerical approach employs the MeteOcean forecasted waves within SWAN and SWASH models (both in 2-d and 1-d mode). The combination of multibeam and d-RTK surveys with Unmanned Aerial Vehicle (UAV) imagery provides high resolution depth grid (0.015 m), particularly required in shallow waters, where wave hydrodynamics is highly influenced by the bottom. The results show a good agreement between video measurements and 2-d predictions of runup. A sensitivity analysis of the Manning's roughness factor is needed in 1-d simulations. The accuracy of the empirical formulas in predicting wave runup in an embayed beach is also investigated, showing mainly overestimation of the observations.

Keywords: Wave runup; Video monitoring; UAV; SWASH ; Runup empirical formulas.

*Corresponding author
Email address: n.valentini@brgm.fr (Nico Valentini)

1. Introduction

1.1. Background

Storm surges represent one of the most significant processes in coastal risk assessment models. They greatly influence exposure of coasts to flooding and erosion, recently intensified by climate changes. In swash zone the in-depth knowledge of storm-induced interactions between morphodynamics and hydrodynamics is needed, since sediment transport highly depends on wave up-rush and back-wash, including groundwater behaviour (e.g., Elfrink and Baldock, 2002; Brocchini and Baldock, 2008; Saponieri and Damiani, 2015). In coastal applications, flooding extent is determined by predicting wave runup, which determines the overwash areas. In such a dynamic coastal environment, despite storm surge can be easily deduced from gauge measurements, wave-induced runup estimation is not so feasible. Available approaches for meeting data collection challenges in such a dynamic coastal environment could be based on the use of remote ground-based observations, numerical modelling and empirical formulas. Numerical models allow to accurately simulate wave propagation from deep-water to swash zone, but they need to be appropriately calibrated under site-specific conditions. In such a context, high-resolution mapping of topography plays a crucial role, since both wave propagation and energy dissipation are strongly influenced by the bottom.

The traditional techniques useful for representing the foreshore Digital Surface Model (DSM), such as Light Detection and Ranging (LiDAR) and Terrestrial Laser Scanner (TLS), provide wide coverage and good accurate topography. However, they involve high costs, long processing time and are often limited by logistic constraints. The use of Unmmanned Aerial Vehicles (UAVs) represents a new approach to survey relatively large areas in less time and with lower operational costs than standard methods, without affecting the accuracy level in digital land mapping (e.g., Harwin and Lucieer, 2012; Gonçalves and Henriques, 2015; Turner et al., 2016). UAVs make beach recognition more feasible for numerical studies, allowing coastal topography to be easily surveyed before and

after a storm event with fewer economic and technical limitations. Only few operational constraints still remain, related to environmental conditions (i.e. wind speed) and the difficulty of placing validating artificial GCPs on such irregular areas.

The availability of detailed topography and field data aimed at calibrating numerical models is not always possible. Over the last half century, different field and laboratory studies focused at collecting wave runup data in several conditions, including sandy beaches as well as structures, by providing a comprehensive dataset for runup parametrization and a practical predictive tool. Most of the empirical formulations relate the wave runup process to deep-water significant wave height, peak period and foreshore beach slope (e.g., Hunt, 1959; Holman, 1986; Mase, 1989; Nielsen and Hanslow, 1991). Efforts have been particularly directed towards quantifying the influence of beach slope on runup estimation, mainly based on the use of an average beach gradient able to approximate the foreshore slope, greatly influenced by morphological changes during storms (e.g., Ruggiero et al., 2001; Stockdon et al., 2006; Bouvier et al., 2017) . Nonetheless, the embayment system, featuring the field area here investigated, differs from the beaches where large part of the parametrisations and were built and validated (e.g., Vousdoukas et al., 2009; Soldini et al., 2012).

1.2. Objectives and Outline

The present work plans to examine the influence of the beach morphology implementation, at an embayed sandy beach, on wave runup predictions during storm events, characterised by rough hydrodynamic conditions. Methods based on both numerical and empirical modelling are implemented. In addition, the aim is to draw up instruments for coastal and maritime management and planning.

The study area is presented in Section 2. Measurements from video system and topographic field surveys are used as benchmarks, as described in Section 3 and Section 4. Wave-induced runup is estimated by means of a numerical chain (Section 5), by one-way coupling the spectral 2-d SWAN with the non-

hydrostatic 2-d SWASH model, forced offshore with MeteOcean waves forecast data. The nearshore topography derives from a proper combination of Multibeam and d-RTK surveys with a Digital Surface Model reconstructed using UAV imagery (Section 3), providing a high-resolution two-dimensional grid. The accuracy of the numerical predictions is then evaluated using the obtained results with measurements derived from the video system and described in Subs. 6.1. Then, the measurements are used to test the empirical formulas in Subs. 6.3. Besides the formulas most used in practice, the models of Mayer and Kriebel (1994) and Mather et al. (2011) are also considered in the present study, due to their peculiar approaches implemented for runup estimation, mainly based on different evaluations of beach slopes and wave parameters. In order to assess the accuracy of runup predictions in 1-d mode, a sensitivity analysis is reported which involved varying the Manning's roughness coefficient, ranging from 0.009 to $0.046\,s/m^{1/3}$, according to the most typical relevant field values for fine-medium sandy beaches (see Subs. 7.1). The main discussions and conclusions are highlighted in Sections 7 and 8.

2. Study area

The study area is located in the South of Italy, in the centre of the embayed beach at Torre Lapillo, hamlet of Porto Cesareo (Lecce). The Marine Area of Porto Cesareo is constituted by the typical sub-environment of low-lying coasts, with calcarenitic rocky and sandy beaches. The latter are characterized by a mean diameter D_{50} equal to $0.47\,mm$ and a D_{95} of $1.38\,mm$. The embayed beach of Torre Lapillo has an asymmetric planform, characterized by a quite strongly curved zone to the NW, a gently curved centre and a relative straight section to the SE (see Figures 1a and 1b).

This coastal stretch has been densely urbanized, since the early 1960's, with remarkable damages to the emerged beach, where the dune was almost totally dismantled, leading to significant erosion. Moreover, in the period 2009–2011 an increase in the mean sea level (by about $13\,cm$) was estimated (Bruno et al.,

2014), contributing to shoreline retreat. In particular, the shoreline erosion hot-spots are located in the south-east, where surveys deployed in 2013-2015 showed an average reduction of the emerged beach width of about 10 m, with respect to 2009.

Most of the time (49.7 %) waves approach from the SSE direction, while for 34.8 % they come from SW. The wave climate is moderate to low, with a significant wave height of less than 0.75 m for 44 % of observations in 2006-2013, compared to 12.17 % for $0.75 < H_s < 1.75\,m$ and only 0.66 % with $H_s \geq 3.0\,m$. The peak period T_p ranging from 3 to 5 s represents the most frequent (about 31.9 %). Due to the diurnal microtidal regime along the Ionian Sea, the tidal range is less than 0.3 m.

In December 2015, a new video coastal monitoring system was deployed and integrated into the Apulian Region Monitoring Network, managed by the local Basin Authority (AdBP), in order to study both morphodynamic and hydrodynamic processes (Valentini et al., 2017a,b). It consists of two visible cameras, framing an area of about 1 km^2. A new Shoreline Detection Model (SDM) for image processing was developed, aimed at extracting shoreline from Timex oblique images, mainly based on the recognition of sea/sand contours from automatic segmented areas (Valentini et al., 2017c). Images are automatically processed and results shared in quasi real-time on a web-portal (`http://91.121.30.84/`). The SDM was calibrated and tested with successful results, making the system suitable for further investigations such as wave runup monitoring, by extracting from videos the leading edge of the wave up-rush on the beach face through semi-automated routines, with a minimum of human guidance.

3. Topographical surveys

Both the emerged and submerged beach in the nearshore zone were surveyed by means of different techniques, to obtain a high resolution DSM of the study area. Transect surveys using differential GPS solutions (d-RTK) on the Global

Navigation Satellite System (GNSS) of Apulia region were carried out just before the two storms considered, i.e. on 1^{st} March 2016 and 9^{th} May 2016. Cross-shore beach profiles were surveyed up to a depth of around 0.9–1 m, on 12 and 16 transects, spaced 10 m apart, in the area framed by the two cameras. Dataset quality was evaluated in terms of both horizontal and vertical accuracy overall the sampled points, with a Root Mean Square Error (RMSE) of 0.0067 m and 0.013 m, respectively. The nearshore submerged beach was derived from a survey using MultiBeam EchoSounder technology (R2 Sonic 2022), conducted by the management consortium of the Protected Marine Area of Porto Cesareo, under flat wave conditions.

The emerged area framed by one camera ($\approx 10,000\, m^2$) was also surveyed by means of an Aeromax 300 multicopter (Microgeo S.r.l., Florence, Italy). The aircraft was equipped with a Sony α5000 camera, featuring an Exmor™APS HD, 20.1 Mp CMOS sensor. The acquisition at 30 m above the ground level and the camera focal length set equal to 16 mm, gave images with a spatial resolution of 0.44 cm.

The UAV imagery was processed by using Structure from Motion (SfM) methodology (e.g., Westoby et al., 2012), which generally proves to be very suitable for environments where a great variability of contrast and prevalent histogram bands occur. Nevertheless, on beaches facing the Ionian Sea, the characteristic features of low vegetated dunes, small-sized ripples and algal blooms makes UAV surveys challenging.

The SfM algorithm is included in several software packages, coded in different forms, typically based on up-to-date routines of computer vision. The friendly and useful interface of Agisoft Photoscan software (v.1.2.4, build 2399) was chosen for the analyses, due to its suitability for UAV image post-processing. In the present study, a mean of 13 overlapping images, taking into account the recommendations of Fonstad et al. (2013), enabled an accurate topographical reconstruction. After the image manipulation process (SfM), bundle adjustment was performed for the dense point cloud reconstruction. The residual errors of the transformation, computed on the GCPs, resulted in $RMSE$ of 0.017 m in

the East, $0.018\,m$ in the North and $0.011\,m$ in the vertical direction. The overall total error (3D) was calculated equal to $0.027\,m$, corresponding in the pixel space in an average value of $0.3\,pixel$ error, with a single outlier of $1.4\,pixel$. A dense point cloud was produced, by using the *high* quality parameter and *aggressive* depth filtering option and then interpolated by the Inverse Distance Weight interpolation method (IDW), to obtain the DSM (Figure 2). The pixel spacing was chosen on the basis of software estimated resolution ($0.0152\,m$), derived from the averaged distance between points within denser areas. Figure 1a shows the emerged study area, marked with a black dashed line, the Ground Control Points (GPCs), the Validation Points (VPs) used for geo-referencing images and validating the DSM, respectively, and the final DSM.

To assess the vertical accuracy of the UAV-derived DSM, the arithmetic average and the Root Mean Square of Differences (RMSD) were calculated, based on the difference between the orthometric heights measured by RTK/GNSS (VPs) and the elevations derived from the DSM at the same horizontal coordinates. The average difference of $0.033\,m$, is comparable with the absolute vertical accuracy of the GNSS points ($0.013\,m$) and in good agreement with previous studies (e.g., Lee et al., 2013; Mancini et al., 2013; Long et al., 2016). Figure 3a shows the comparison between the elevation of VPs (z_{DGPS}) and the corresponding points extracted from the DSM (z_{UAV}). The regression line shows agreement between measurements, with a fitted line slope close to 1 and R^2 equal to 0.995. In Figure 3b the frequency histogram of the differences $\Delta_z = z_{UAV} - z_{DGPS}$ is reported. The $RMSD$ ($0.044\,m$) is almost equal to the mean value, with a narrow amplitude of the variation, with only one significant outlier, at approximately $0.12\,m$. These validation procedures show average discrepancies at the centimetre order, due to a combination of factors: (i) ground control and validation points were surveyed with d-RTK using reference stations, with their own vertical accuracy ($0.013\,m$); (ii) target points located with care using a plane base under the GPS pole can introduce errors due to movement of the sand; (iii) the interpolation procedure for DSM reconstruction often results in artefacts (i.e. ripples of a few centimetres) in a highly-corrugated sandy en-

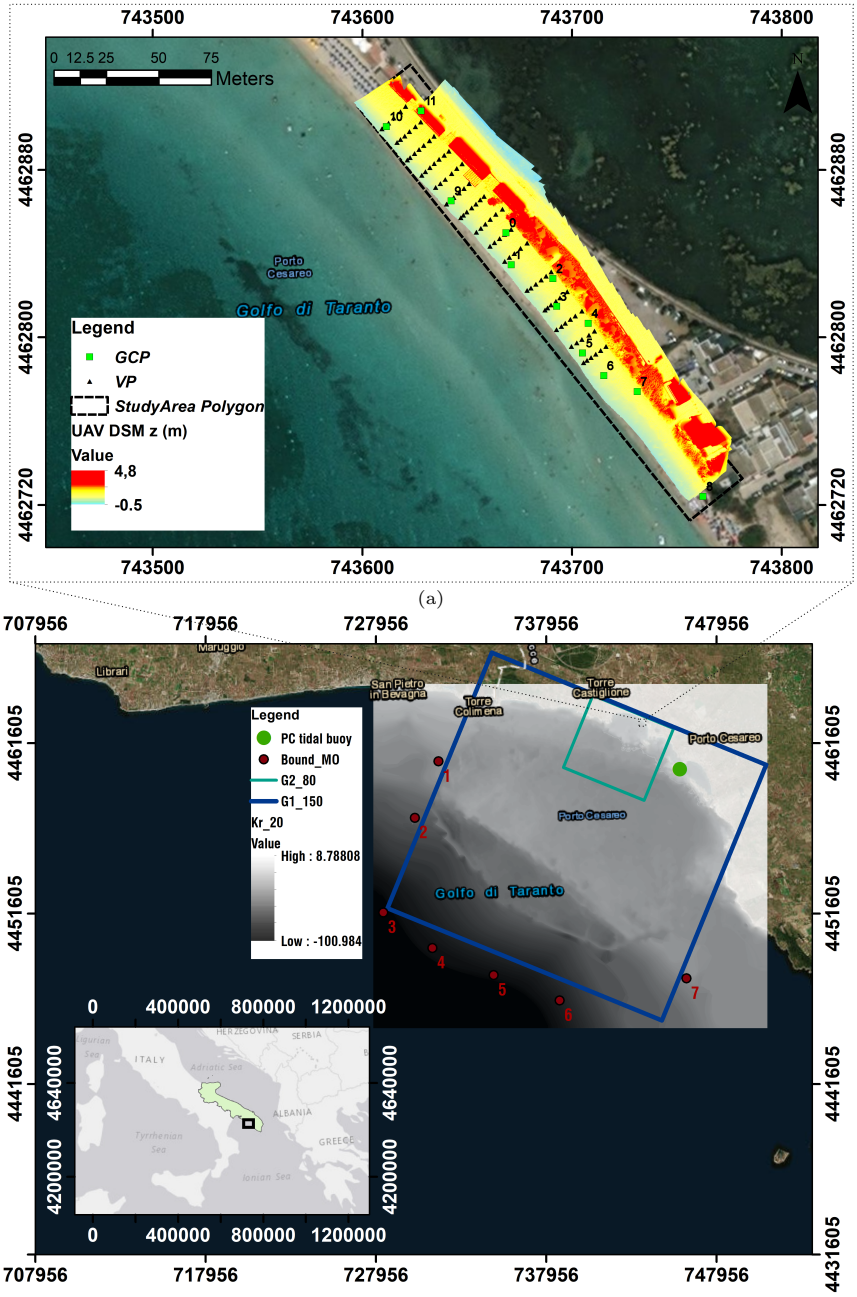

Figure 1: (a) DSM obtained from UAV survey. Elevations above sea level measured in m. Highlighted the GCPs location; (b) bottom grid derived from Robust Kriging interpolation with nested grids G_{150} (blue contour) and G_{80} (light green contour); tide gauge (green dot) and MeteOcean boundaries locations (red spots). The inset map highlights the field study area representation. (colour image)

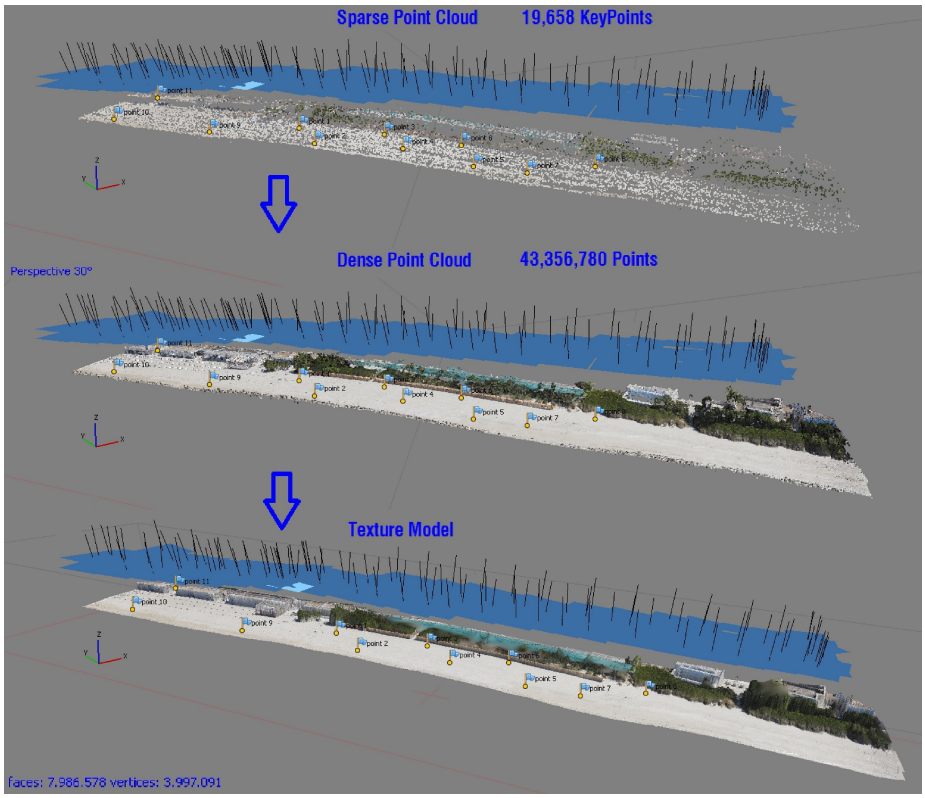

Figure 2: Photogrammetric process at the Torre Lapillo beach; top: creation of sparse point cloud; middle: dense point cloud; bottom: model texture (the reference number on the left bottom of each 3-d sketch defines the KeyPoints and faces/vertices). (colour image)

vironment; (iv) the different techniques employed for both surveys are based on remote imagery and intrusive rod acquisitions. Despite these differences, the survey successfully met the requirements for topographic monitoring of common sandy beaches.

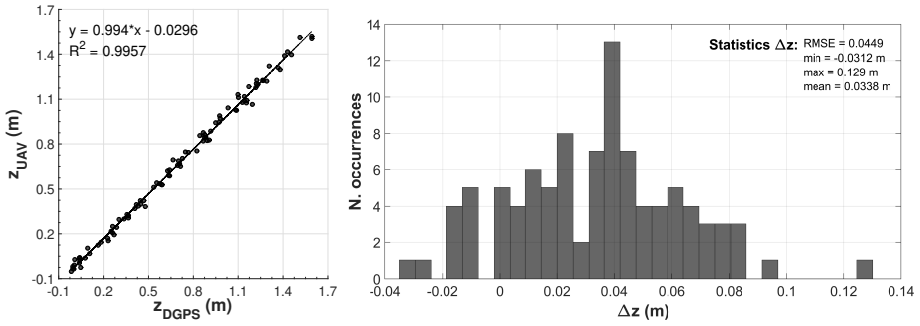

(a) (b)

Figure 3: (a) Comparison between the elevation of VPs GNSS data and corresponding points extracted from the UAV DSM. Linear fitting plotted and regression parameters highlighted; (b) frequency histogram for classes of 2 cm and bulk statistic parameters of differences. (b/w image)

4. Runup measurement from video recordings

Timestack images for wave runup measurements (e.g., Holman and Stanley, 2007; Salmon et al., 2007) were generated in correspondence of two significant storm events, occurred in March and May 2016. Each video had a duration of $30\,min$ with a frame-rate frequency of $5\,Hz$. The image geo-rectification took place, after a lens distortion correction, by applying a 3×4 perspective transformation matrix, using homogeneous coordinates (Vousdoukas et al., 2014). The pixel intensities were extracted along the selected cross-shore transects from each frame during video progressions with Python scripting and OpenCV libraries. Timestack pre-processing is crucial before implementing routines for swash oscillations recognition, also due to the presence of objects on the beach in the camera's Field of View (FoV) (e.g., geo-textile sand bags, algae, flags, etc.), resulting in dirty or altered images. Moreover, while the wave up-rush on the beach face can be easily identified as a clear feature and easily extracted through semi-automated routines, the backwash phase is less distinguishable, do to the saturation of the sand . The edge identification approaches, colour or texture-based, could instead tend to discern the upper envelope of swash motions, particularly for beaches featured by mild to high foreshore slope.

The pre-processing procedure dealt with the masking of the fixed objects visible in the camera FoV, by manually sampling the first frame and applying an automatic inpainting of the following ones, before creating the timestack. Furthermore, a combination of filters was applied in the following order: background subtraction (Gaussian Mixture-based); Bi-Exponential Edge-Preserving Smoother (BEEPS, Thévenaz et al. (2012)); variance filter on the grey-coded channel.

The processing of the timestack edges (wave-by-wave) was then performed using MATLAB-based open-source software, GUI-timestack (https://sourceforge.net/projects/guitimestack/), in order to extract and process the swash time series (Vousdoukas et al., 2012), based on modified Otsu's thresholding method (Otsu, 1979). Final timestack images, re-sampled at $2.5\,Hz$ for easier post-processing, had a cross-shore resolution in the range of 2–15 cm, derived from the minimum pixel footprint values along each transect. Figure 4 reports an example of the cross-shore transect location for the calculation of video-derived runup (a) and the relative timestack (b) with the time-variation of the swash leading edge (red line) and the swash extremes.

Cross-shore coordinates of swash extremes were then converted into water-level elevations time series using topographical information derived from the surveys, by assuming negligible morphological changes between video acquisition and d-RTK GPS surveys, performed 2 days before the storm events. The estimated elevations represent the total runup, $\eta_{tot}(t)$, defined as follows:

$$\eta_{tot}(t) = \eta_{tide} + \eta_{su} + \eta_s + S_{sw}(t) \tag{1}$$

where η_{tide} and η_{su} are the tidal and surge heights, respectively, η_s is the maximum wave setup and $S_{sw}(t)$ is the swash-induced water-level fluctuation (Stockdon et al., 2006; Vousdoukas et al., 2009). The wave runup R was derived from the peaks of water level fluctuations $\eta_{wl}(t)$ time series with respect to the still water level (Eq. (2)):

$$\eta_{wl}(t) = \eta_s + S_{sw}(t) \tag{2}$$

(a)

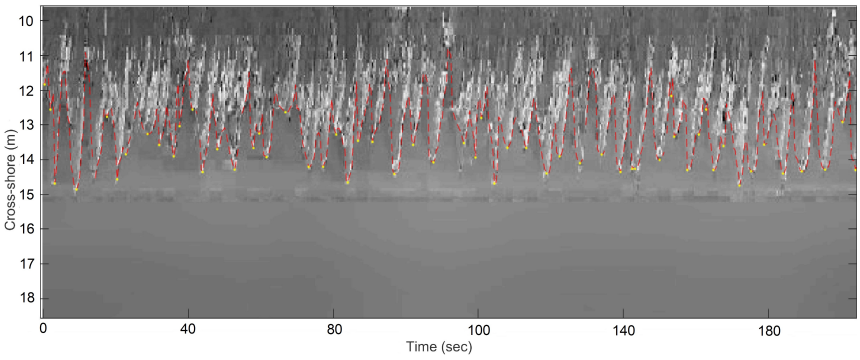

(b)

Figure 4: (a) Example of cross-shore transect for runup measurement (red dashed line); (b) processed timestack, x-axis and y-axis indicating time and cross-shore distance. (colour image)

In the present study, given the relatively small distance between the tide gauge and the study area ($\sim 2\,Km$), tidal and surge heights were assumed to be known since they were directly measured. The runup statistics were calculated for both events, by considering the maximum value of the time series (R_{max} and the 2% exceedance values derived from the cumulative probability density of runup maxima elevations ($R_{2\%}$).

5. The numerical chain

The numerical approach deals with computing waves approaching the nearshore including the surf zone using the SWAN model (Booij et al., 1996). Initial and boundary conditions were derived from the MeteOcean forecast reanalysis database (Mentaschi et al., 2015), for both storm events considered. The non-hydrostatic SWASH model (Zijlema et al., 2011) was then applied to solve the NSWE until the shoreline for evaluating swash processes. The proposed strategy of one-way nesting MeteOcean forecasted waves into the SWAN model rather than directly into SWASH, allows a good representation of the wave processes to be achieved on meso/fine-scales. The capability of SWAN to produce very accurate shallow water spectral wave conditions, ideal for SWASH implementation, is indeed extensively known and tested. SWASH was chosen since in the literature it is revealed to be numerically more straightforward than similar phase resolving models, in terms of numerical robustness (De Roo et al., 2015), ease of implementation and open source orientation (Celli et al., 2018). Shallow water equations were firstly solved on both 1-d and 2-d domains, for the storm event Ev_2, recorded by camera PC_{vs2} thanks to the availability of the UAV survey, in order to assess the sensitivity of the model to the spatial domain dimension. Then 1-d SWASH simulations were performed for both storm events (Ev_1, Ev_2), to test the influence of roughness coefficient on numerical results.

5.1. SWAN model

SWAN model set-up includes spectral waves modelling in non-stationary mode, by using two nested regular grids (Table 1). The coarser offshore grid, 16.2 km long and 17.4 km wide, started at a depth of around 90 m. From a depth of approximately 35 m until the shoreline, wave transformations were analysed on a nested finer regular grid, 4.5 km long and 5.1 km wide (Figure 1b). The bottom grid was derived from a Robust Kriging interpolation of the offshore bathymetry and the Multibeam Echosounder survey of the nearshore, with a final resolution of 20 m.

Table 1: Computational SWAN grid features (Cartesian coordinates).

GRID	RESOLUTION	x_o	y_o	DIR_x	$m_x * m_y$
G_{150}	150 m	728722.8	4451961.1	338°	$115 * 107$
G_{80}	80 m	739010.1	4460207.1	338°	$63 * 56$

Wave boundary conditions were derived at 7 points from the MeteOcean forecast wave database, resulting from the WaveWatchIII model applied in the Mediterranean Sea. The model, developed and maintained by the DICCA Department of Genoa University (Italy, http://www.dicca.unige.it/meteocean/) is characterized by a high accuracy level in wave forecasting. The dataset includes the wind speed and direction as well as the main bulk spectral parameters in terms of significant wave height (H_s), peak period (T_p) and mean wave propagation direction at the peak period (Dir_p). A time step of 30 min was used, with wave boundary condition data included every hour, for a total computational time of 20 hr, around the time of observations. Tidal data refer to water levels measured at the nearest Porto Cesareo tide gauge.

Figure 5 reports an example of the boundary bulk spectral parameters and the sea levels, at point N. 5 on the SW boundary (Figure 2). In all graphs, vertical dotted red lines indicate the time of runup measurements.

The spectral space was computed at 24 equally spaced propagation directions ($\Delta\theta = 15°$) and 24 logarithmically spaced frequencies between 0.04 Hz and 0.6 Hz. For the physics, the default parameters are used (breaking constant, JONSWAP formulation of friction, setup, diffraction and triad interactions included, without considering the quadruplet interactions parameter). Wind forcing was not considered, because of the quite small geographic size of the computational domain.

5.1.1. SWASH model

Event Ev_2 was simulated by SWASH in two-dimensional non-hydrostatic mode, over a curvilinear grid (205×1346 grid points). Stationary conditions

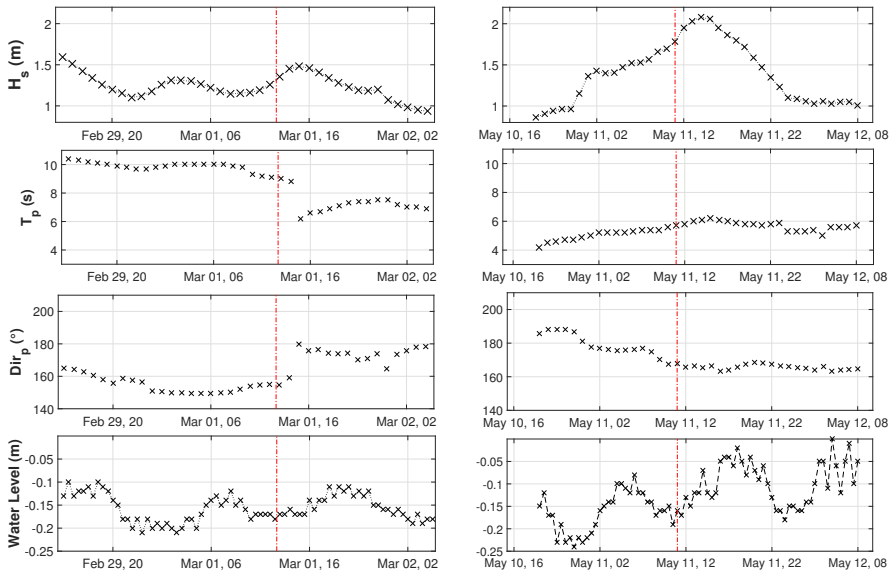

Figure 5: Boundary bulk spectral parameters from the MeteOcean model, computed at the point N. 5, and the relative sea level measured by the PC tide gauge for the two storm events. (colour image)

were assumed (Guimarães et al., 2015). The bottom was generated by merging the Multibeam dataset, with the d-RTK surveyed cross-shore transects and the UAV-derived Digital Surface Model, with a resolution of $0.1\,m$. The computational domain spanned $203\,m$ along-shore and $750\,m$ cross-shore, with a computational grid resolution equal to $1\,m$ and 0.13–1 m, respectively (Figure 6).

Wave spectral conditions were set at each open boundary from the time dependent energy peak derived from SWAN spectral results and the mean water level condition imposed from PC tide gauge measurements. The simulation time was $35\,min$ with a spin-up time of $5\,min$ and a time step of $0.008\,s$. Runup temporal statistics ($R_{2\%}$ and R_{max}) were derived by tracking the wet/dry interface, obtaining the cross-shore temporal variation of water levels at a single longshore location.

Figure 7 shows an example of the spatial variability of SWASH water-level

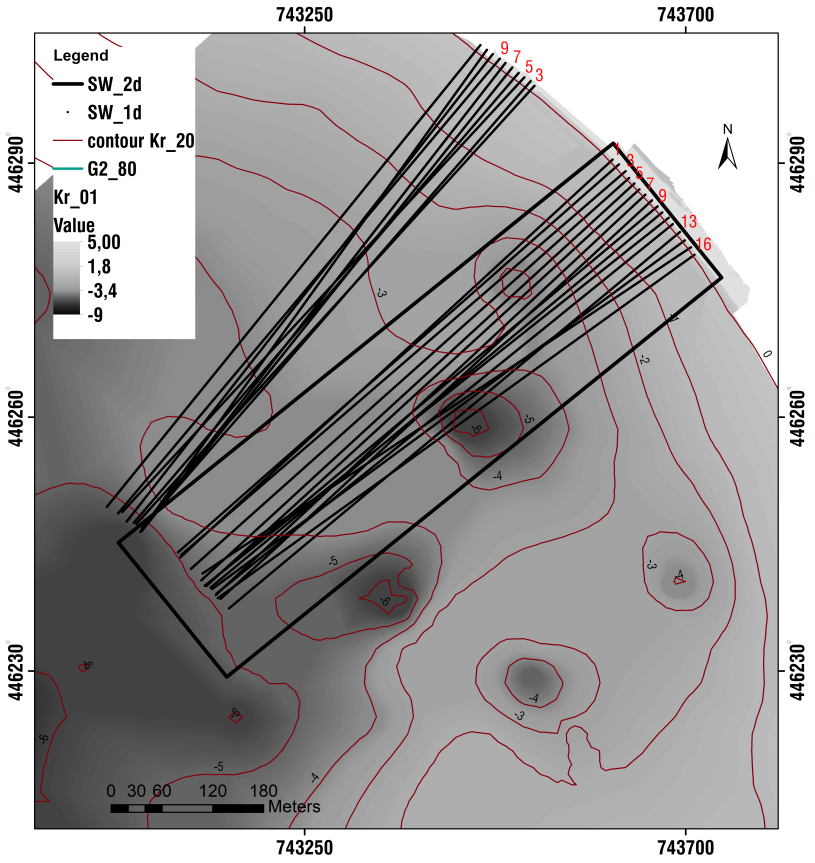

Figure 6: SWASH 2-d model boundary (black rectangle) and 1-d transects (black). The contours of the bathymetry Kr_{20} and the raster of Kr_{01} are represented. (colour image)

computed after 6 min of simulation and the corresponding timestack. For flooding calculations SWASH considers a time-varying moving shoreline, influenced by the friction coefficient (e.g., Svendsen, 2006; Antuono et al., 2012). In the present work, the Manning's formulation was used for bottom friction with its default value ($c_f = 0.019$).

In order to investigate 1-d SWASH predictive accuracy, the swash zone hydrodynamics were simulated for the two storm events at 16 cross-shore transects (Figure 6), by assuming along-shore uniformity. Computational 1-d grids were derived from RTK-GPS surveys and nearshore Multibeam bathymetry, with a

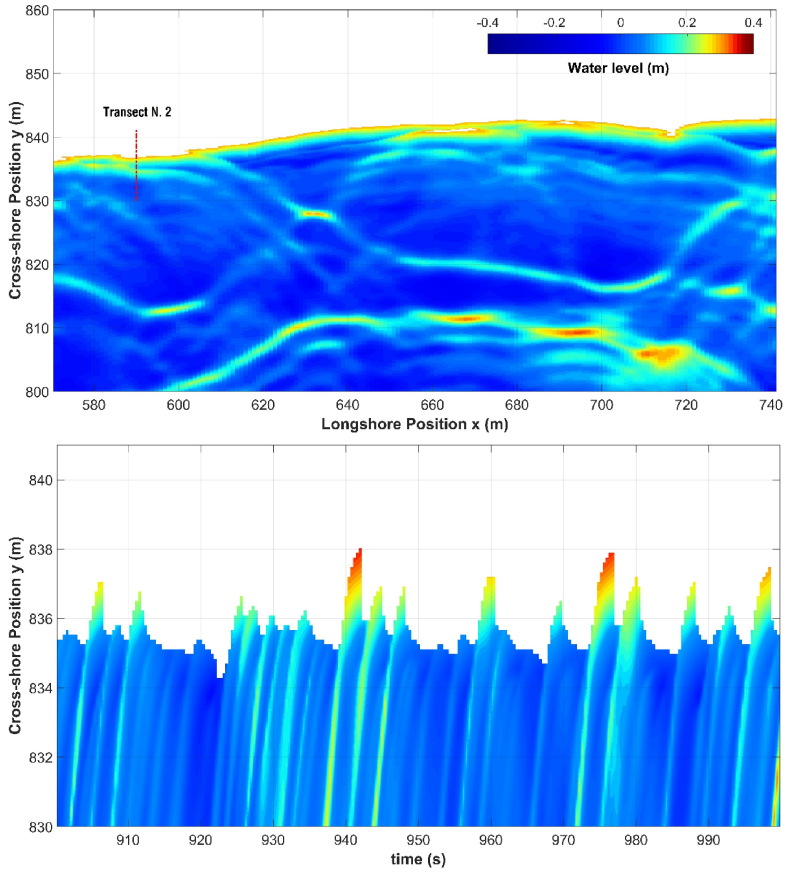

Figure 7: Top: Plan view showing the spatial variability of SWASH water-level computed at 6 min time step (Ev_1); bottom: the timestack shows a portion of temporal cross-shore variation of SWASH water levels at Transect N. 2 (Origin of reference Coordinate system: [x,y]=[7.435838e+05,4.4624715e+06]). (colour image)

mean length of 700 m and a grid step of 0.13 m and 0.05 m for transects within the field of view of the first and the second cameras, respectively. The simulation time for each transect test case was set to 35 min with a time step of 0.014 s. The outputs, after a spin-up time of 5 min, were requested every 0.4 s, consistent with the timestack time discretization. The default minimum and maximum Courant numbers were kept at 0.4 and 0.8, respectively, as in the 2-d case. During each simulation the mean water level condition was imposed by

considering the water level measured by the PC tide gauge. Wave spectral conditions were set at the open boundary points of the computational grid domains, derived from the time dependent energy peak of the SWAN spectral results.

6. Results

6.1. 1-d and 2-d SWASH modelling

Figure 8 shows the comparison between predicted and measured 2% exceedance and maximum wave runup in correspondence with cross-shore transects where numerical and video-measurements outputs were both valid, in the 2-d as well as the 1-d approach, for the storm event Ev_2. The accuracy of the model is evaluated by the the Root Mean Square Error (RMSE, Eq. (3)), the bias (Eq. (4)) and the percent error, ($Perc\_Err$, Eq. (5)), defined as follows:

$$RMSE(x) = \sqrt{\frac{1}{N}\sum_{i=1}^{n}(x_{i,predicted} - x_{i,measured})^2} \tag{3}$$

$$bias(x) = \frac{1}{N}\sum_{i=1}^{n}(x_{i,predicted} - x_{i,measured}) \tag{4}$$

$$Perc\_Err = \frac{x_{i,predicted} - x_{i,measured}}{x_{i,measured}} \times 100 \tag{5}$$

The comparison of the predicted 2-d values with respect to the corresponding observations shows a mean $Perc\_Err$ of $R_{2\%}$ (R_{max}) equal to $-10.9\,\%$ ($-13.3\,\%$), a maximum of $32.3\,\%$ ($38.4\,\%$) and a minimum of $-4.3\,\%$ ($-8.2\,\%$). In general, the $R_{2\%}$ was better predicted than the R_{max} with an RMSE equal to $0.084\,m$. The numerical results show a small tendency to underestimate measurements, as confirmed by the negative value of BIAS ($-0.056\,m$). Greater differences can be observed in the computation of R_{max} with an RMSE equal to $0.156\ m$. Differently from the $R_{2\%}$, for which the differences between measured and predicted values are quite the same overall the selected transects, the R_{max} was particularly underestimated for the central cross-shore transects. Such a general trend must be partially motivated by the vertical accuracy of the

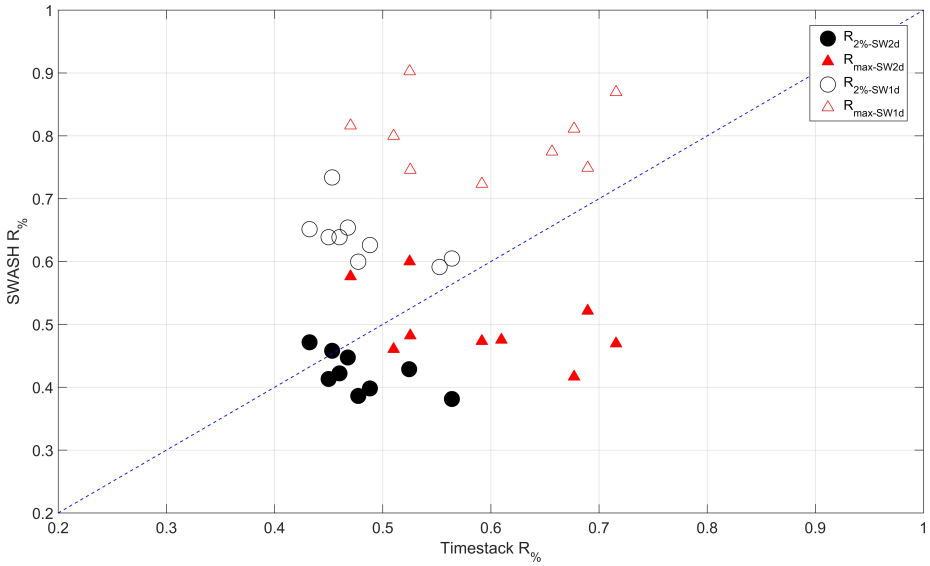

Figure 8: Predicted and measured $R_{2\%}$ and R_{max} for both 1-d and 2-d spatial domains over 9 transects, in the area framed by camera PC_{vs2}. (colour image)

UAV-derived DSM, where systematic discrepancies with respect to ground-truth GNSS data, are about $0.03\,m$.

With regard to 1-d modelling, the same Figure 8 highlights the comparison between 1-d model predictions of runup with respect to the actual video measurements. Since the along-shore components of bathymetry, wave groups, and swash oscillations are not fully resolved, 1-d swash levels higher than 2-d ones are to be expected (Stockdon et al., 2014).

In general, the mean difference, in terms of $Perc\_Err$, was equal to 30.21 % for $R_{2\%}$ and 34.1 % for R_{max}, while the maximum difference of $R_{2\%}$ (R_{max}) was equal to 74 % (73.6 %), and the minimum was 25 % (0.5 %). Considering the transects investigated, the variance of these differences was actually low, hence relevant alongshore variability was negligible.

6.2. The influence of the Manning's friction

A sensitivity analysis of the SWASH model capability in predicting nearshore hydrodynamics was performed by varying the Manning's roughness factor from

0.009 to 0.046 $s/m^{1/3}$, according to the most typical relevant field values (Benson and Dalrymple, 1967). Figures 9 and 10 show the predicted $R_{2\%}$ and R_{max}, respectively, adimensionalized by the offshore significant wave height, as a function of the bottom friction coefficient (a), with the relative mean differences and
350 $RMSE$ (b) over all the selected transects.

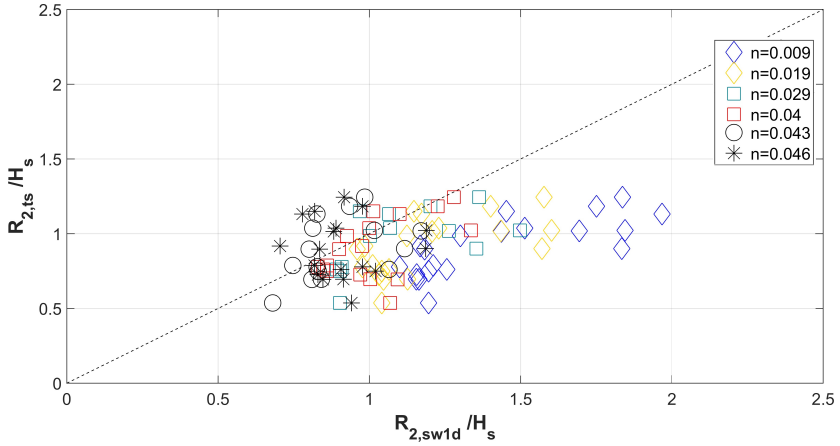

(a)

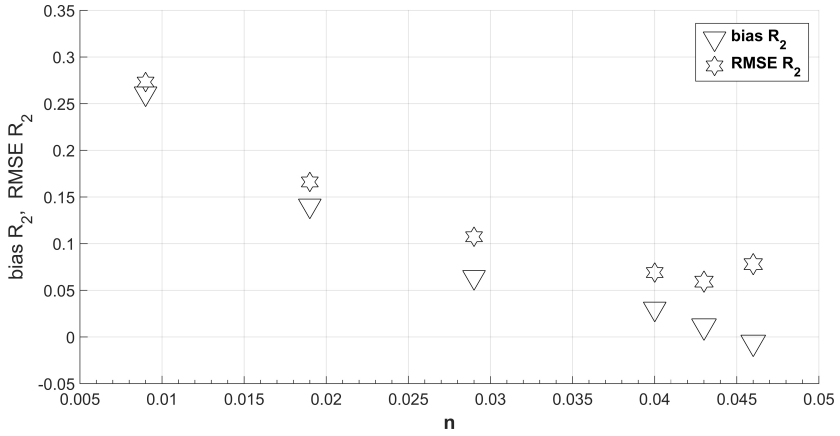

(b)

Figure 9: (a) Predicted and measured $R_{2\%}$ for transects analysed, both quantities are normalized to the significant wave height at relative boundary; (b) sensitivity of computed $R_{2\%}$ to bottom friction coefficients. (colour image)

Specifically, the values $n = 0.043\, s/m^{1/3}$ and $n = 0.04\, s/m^{1/3}$ reveal the best

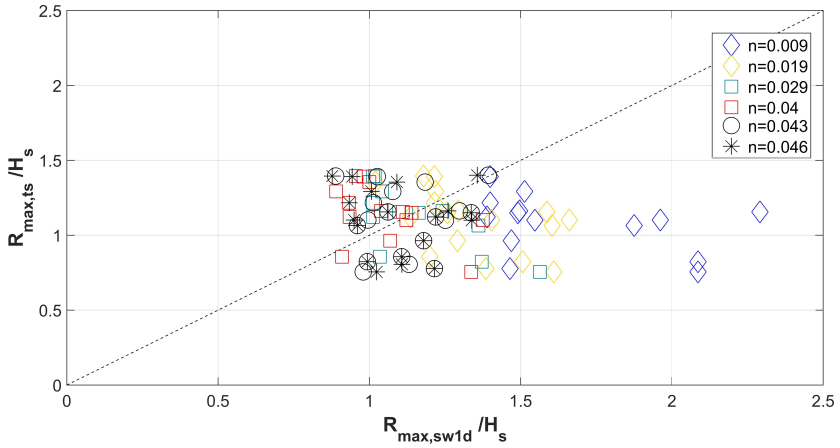

(a)

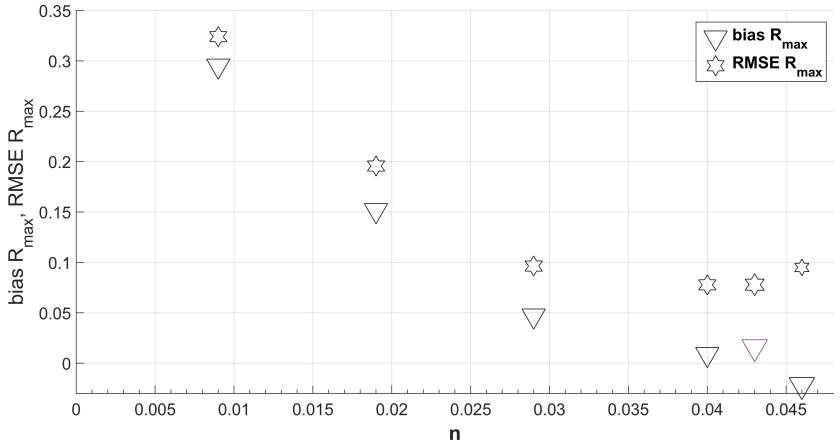

(b)

Figure 10: (a) Predicted against measured R_{max} for transects analysed, both quantities are normalized to the significant wave height at relative boundary; (b) sensitivity of computed R_{max} to bottom friction coefficients. (colour image)

fit in predicting the timestack measurements, with respect to $R_{2\%}$ calculation and to R_{max}, respectively. For the first variable the $RMSE \cong 0.05\,m$ and the $bias \cong 0.018\,m$, while for R_{max}, $RMSE \cong 0.075\,m$, and $bias \cong 0.01\,m$. With respect to the 2-d simulation, where the model achieves optimal performance in runup prediction with the default friction coefficient, the 1-d results are satisfying only with an ad-hoc calibration. In fact, the infragravity component of

the overall spectral wave energy has been previously reported to be often overestimated by the SWASH model (1-d), particularly in the surf zone (Zijlema et al., 2011; Conde-Frias et al., 2017). This overestimation mainly depends on the standing-wave component caused by reflection of infragravity waves close to the shoreline (Zijlema and Stelling, 2008), together with errors associated with the bottom friction estimate, which acts as a primary mechanism by which the longer waves lose energy (Smit et al., 2014), and finally on the not fully solved alongshore components of the hydrodynamic processes, which affect dissipation processes in the swash zone.

6.3. Empirical runup

This subsection contains the results of the empirical runup formulations for the storms considered, when reliable corresponding measurements were available. A total of 8 models, well described in literature (Atkinson et al., 2017; Vousdoukas et al., 2012) are tested and discussed. The models used have been found to be the most accurate for the data sets upon which they were built (Atkinson et al., 2017) and they can be considered the most useful in practice for most applications in coastal engineering. Among them, the model from Mather et al. (2011) has been applied, which highlighted the importance of using not only the foreshore slope, but also the bathymetric profile until the closure depth, Eq. (6):

$$R_{max} = C H_0 S^{2/3} \tag{6}$$

where S acts as a representative nearshore slope and C is a dimensionless coefficient which takes into account the beach morphology. Their model is supported with $C = 10$ for open beaches, while it required an adjustment of the coefficient for large ($C = 9$) and small ($C = 6$) embayments. Moreover, an analytical solution for wave runup over non-uniform beach profiles, discussed in Mayer and Kriebel (1994), is tested, Eq. (7):

$$R = \frac{\beta_f}{2}(X_b - \sqrt{H_o L_o})\left[-1 + \sqrt{1 + \frac{4 h_b \sqrt{H_0 L_0}}{\beta_f (X_b - \sqrt{H_0 L_0})^2}}\right] \tag{7}$$

where the mean runup is derived from a formulation of the average slope between the incipient breakpoint and the runup limit, defined by Eq. (8):

$$tan\beta_{fb} = \frac{R + h_b}{X_R + X_b} \tag{8}$$

Table 2 summarizes the mean values of $R_{2\%}$ and R_{max} over the reliable transects analysed (n.16), representative of the gently curved centre of the large embayed beach of Porto Cesareo. Both quantities refer to the offshore spectral wave parameters (e.g., H_s, L_{0p}, T_p), derived from averaging the MeteOcean model inputs on points N. 4, 5, 6 and 7 in Figure 1b located at the SW boundary of SWAN grid G_{150}.

Table 2: Summary of the runup predictions derived from empirical formulations, as mean values over n.16 transects, for the two storm events Ev_1 and Ev_2 investigated.

	Ev_1	Ev_2	$MeanErrorPerc.$
	$R_{2\%}(m)$		
Timestack	0.49	0.48	-
Holman (1986)	0.92	1.13	109.6 %
Nielsen & Hanslow (1991)	0.88	0.8	71.7 %
Mayer & Kriebel (1994)	0.52	0.56	10.4 %
Ruggiero et al. (2001)	0.93	0.79	75.8 %
Stockdon et al. (2006)	0.97	0.88	89.1 %
Atkinson et al. (2017)	0.94	0.85	83.0 %
	$R_{max}(m)$		
Timestack	0.6	0.59	-
Douglas (1992)	1.23	1.17	101.6 %
Mather et al. (2010)	0.57	0.69	5.8 %

Most of the models investigated greatly overestimate the observed wave runup, both $R_{2\%}$ and $R_{max\%}$, with a mean percentage error of more than 70 %. The models showing the best performance at this embayed system are from

Mayer and Kriebel (1994) and Mather et al. (2011). As also suggested in Stockdon et al. (2006), this bears witness to the fact that runup prediction using deep water buoy measurements may result in significantly higher results than those obtained using a wave height measured at a local buoy (closer to the shore), where nearshore wave processes can be properly taken into account.

7. Discussion

7.1. 1-d and 2-d SWASH modelling

The differences in runup for the two dimensional spaces can be explained by several physical/numerical factors. In order to retrieve reasonable causes for this behaviour some concepts need to be highlighted. It must be noted that the same radiation boundary condition was imposed within the investigated area to simulate entering waves without reflections. The significant wave height modelled in 1-d (red line) and 2-d (blue line) domains are reported in Figure 11, for a representative transect (n.9). Moreover, the wave power spectral density at the representative boundary, breaking and surf representative sections are reported.

The two implementations do not show any substantial difference until the breaking zone, even if the 2-d signal shows higher oscillations which increase approaching the breaking zone. Within the surf zone, greater attenuation is highlighted for the 2-d model, with respect to the 1-d, with consequent differences in runup calculations, due to discrepancies in wave energy propagation modelling.

The SWASH breaking mechanism, here applied, is based on Hydrostatic Front Approximation (HFA) algorithm (Smit et al., 2014), automatically activated when a low number of layers is implemented in the model. The HFA approach is used in both spatial domains. In both domains, before incipient wave breaking, an increase in wave energy occurs. In 2-d domain the energy is mostly concentrated at the peak frequency, wave directionality tends to reduce the forcing waves in the infragravity frequencies (Herbers et al., 1994). In

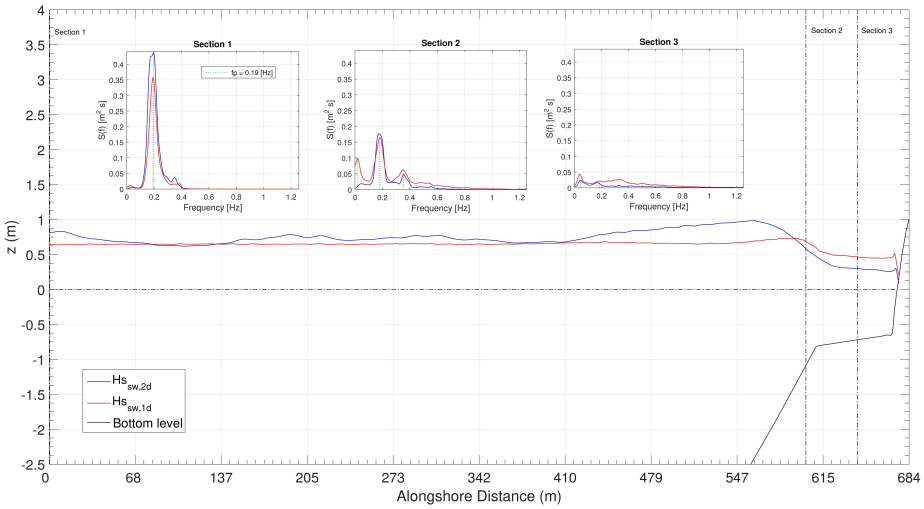

Figure 11: Cross-shore variability of H_s between SWASH 1-d and 2-d and spectral transformation of water levels output comparison for the two spatial domains, at three representative sections (Transect N.9). (colour image)

the 1-d model, instead, the spectrum shows wave energy components at low-frequencies and a reduction of the energy at the peak frequency. In the surf zone, 2-d model spectra mainly highlight the breaking-induced dissipation. In the 1-d spectra infragravity waves are assumed to dissipate by transferring their energy back to higher frequencies, by infragravity-wave breaking (Henderson et al., 2006) and by bottom friction (secondary importance). The higher wave energy content simulated in 2-d induces a seaward shift of the first breaking section, with respect to the 1-d domain, with a consequent broadening of the surf zone.

For this reason, a preliminary analysis using a cross spectral analysis via magnitude-square coherence of runup and surf zone water levels was conducted. A standing-wave component in the infragravity frequencies can be observed in 1-d runs with respect to the 2-d domain. This factor most probably led to such results and is associated with the different highlighted simulated contributions of alongshore dissipation mechanisms of swash via non-linear and frictional processes.

By comparing both the 1-d and 2-d numerical models with the runup measurement derived from video analysis, the results show that the 1-d model systematically overpredicts the timestack results. The influence of the seabed friction, for NLSW equation models, in wave runup prediction and overtopping due to a global damping of the flow, is well-known (e.g., Tuan and Oumeraci, 2010; Suzuki et al., 2011; Antuono et al., 2012). Different formulations are implemented in SWASH for the dimensionless friction coefficient calculation c_f. In the present study, the formula based on Manning's roughness coefficient n is used, Eq. (9):

$$c_f = \frac{n^2 g}{h^{1/3}} \tag{9}$$

The default value for this parameter in SWASH was set to $0.019\, s/m^{1/3}$. Currently, there are not unequivocal results or suggestions available in the literature about its optimal variability. Among several parameters under coastal regime, n mainly varies with grain diameter (e.g., Reis and Gama, 2010). For instance, previous studies (e.g., Suzuki et al., 2011) suggest that the behaviour of smooth materials in the laboratory could be well represented by using a value of approximately $0.01\, s/m^{1/3}$, while a Manning's coefficient equal to about $0.02\, s/m^{1/3}$ is suggested for sandy materials with a diameter close to $1\, mm$, as in the present field case. Due to such a range of variability of the coefficient and the difficulties between field and laboratory measurements, it represents a useful and straightforward parameter for numerical model calibration.

Figure 12 shows an example of the spatial variation of significant wave height derived from the zero-order moment of the spectrum (H_{m0}, Figure 12a) and wave setup (η_s, Figure 12b) for transect N. 6, modelled by SWASH in a 1-d spatial domain, with different bottom friction values. Seaward from the first breaking point, where significant wave height and the setup show their max and min values, neither quantity is very sensitive to bottom friction. This behaviour was observed for all sections analysed. On the contrary within the surf zone area, both wave setup and significant wave height become more sensitive to n because of the increasing bottom effects on propagating waves. No influence of

the friction factor on the wave peak period was observed.

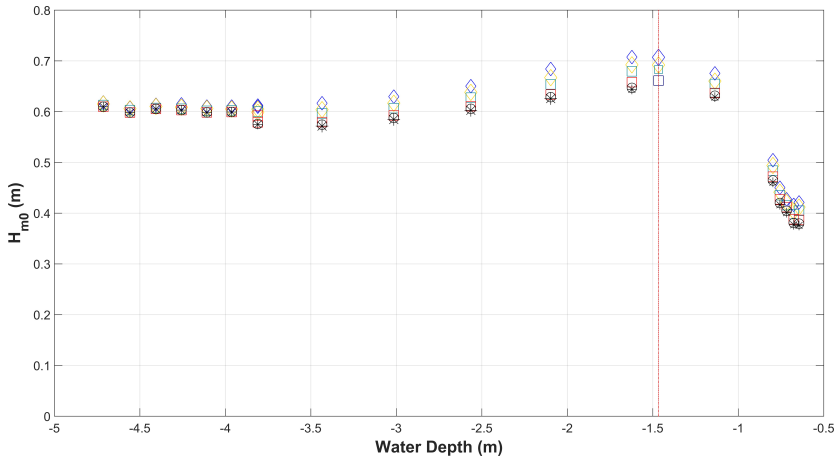

(a)

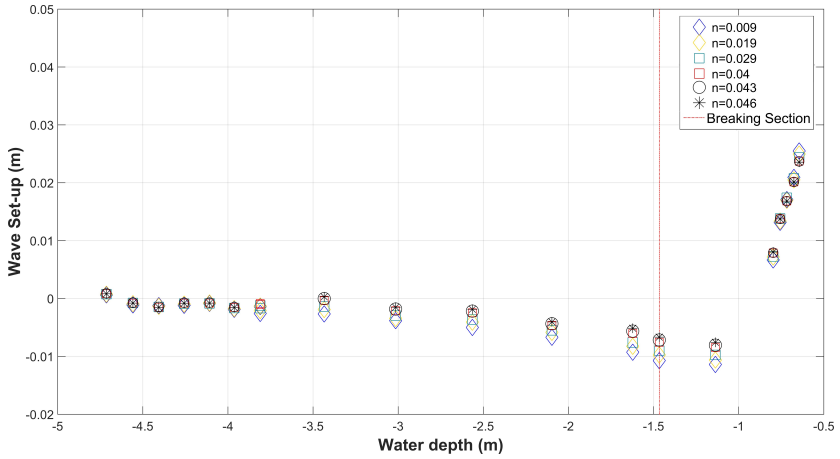

(b)

Figure 12: Sensitivity of significant wave height H_{m0} (a) and wave setup η_s (b) for varying Manning's coefficient. (colour image)

One source of error in SWASH predictions is due to the changes in beach morphology, which are not straightforward to estimate, since submerged and emerged beach were surveyed in different periods. Geoprocessing surveys show that in the zone straddling both GPS and Multibeam, at approximately $1\,m$ depth, the gap over the whole investigated area was less than $5\,cm$. DEM is,

indeed, obtained by neglecting any substantial modification of the submerged morphology. However the seasonal and interannual variability of hydrodynamics may change short-term morphodynamics, by introducing errors in the wave runup propagation and calculation. Despite such limitations, which are very common in practice, the model shows acceptable responses for the events considered, with respect to the video observations.

7.2. Insights on runup formula

Runup studies, upon which most of available empirical parametrisations have been based, have been mainly carried out on open sandy beaches, approached by oceanic swell, extreme storm waves and tide waves even if the formulations are often used in several different morphologies and broad wave climate conditions, providing a wide scatter of results. Few runup studies have been performed on such embayments (Vousdoukas et al., 2009). Predictive models of wave runup, and specifically those investigated in the present work, traditionally focus on the beach foreshore slope β_f as the key determinant of $R_{2\%}$, under both regular (Hunt, 1959; Mase, 1989) and irregular waves (Holman, 1986; Nielsen and Hanslow, 1991; Ruggiero et al., 2001; Stockdon et al., 2006). Whereas, Douglass (1992) argued that the maximum runup is not influenced by the beach-face slope, the model of Nielsen and Hanslow (1991) assumes no dependence on beach slope only for $tan\beta_f \leq 0.1$, as is the case for the majority of the analysed transects, with two exceptions.

As observed during laboratory experiments described in Blenkinsopp et al. (2016), empirical formulas better predict wave-induced runup under controlled boundary conditions since waves are perpendicular to the shore and not affected by wave direction. Moreover, the inundation process on a tideless embayed beach has been demonstrated to be better captured by using the breaking wave height (Sancho et al., 2012). On the other hand, as highlighted in Stockdon et al. (2014), such parametrisations generally suffer from systematic errors, due to site-specific characteristics that are not included in the models. The exception are empirical models whose different and well-fitted performance is largely

explained by the approaches used for the calculation.

As the time of writing, the $R_{2\%}$ evaluated by the analytical solution of Mayer and Kriebel (1994) best agrees with the video measurements for both events, most probably due to the use of the so-called *effective slope* in the runup calculation. The *effective slope* derives from Saville's method (Thorndike Saville, 1957) which introduces, over arbitrary geometries, an appropriate average slope for predicting runup on a composite-slope, and allows the entire active surf zone to be taken into account, between the wave break point and the runup limit, Eq. (8). The $R_{2\%}$, Eq. (7), is then calculated with reference to the distance $X_b(t)$ and the corresponding time series of $h_b(t)$ are taken from 2-d SWASH simulations.

The formulation which best predicts the R_{max} is that of Mather et al. (2011) who correlates the maximum wave runup height with the shape of the offshore profile as well as the foreshore slope. Such an offshore limit is defined until a specified point on the sea bed at a certain distance x_h and depth h seaward of the surf zone, according to the following relationship:

$$\frac{R_{max}}{H_0} = \left(\frac{x_h}{h}\right)^p \tag{10}$$

where p is comparable with the coefficient of power law in Bruun's equilibrium profile (Bruun, 1954). The dimensionless coefficient C in Eq. (6) is assumed to be derived from large embayment condition ($= 9$), while S is referred to a representative nearshore slope, calculated until the closure depth, estimated from the formula from (Birkemeier, 1985), at a depth of $5.4\,m$.

8. Conclusions

The capability of predicting wave-induced runup on an embayed sandy beach by using different approaches has been evaluated in the present work. Video observations are compared with numerical results derived from one-way coupling of opportunely nested SWAN and SWASH models, forced by the MeteOcean

forecast wave data. A non-standard computer vision−photogrammetric technique demonstrated the potential of UAV imagery for deriving a high-resolution, accurate and reliable topographical input, which is particularly useful for fragile and complex coastal areas.

The comparison between 2-d runup predictions and video observations demonstrates an overall good representation of swash zone hydrodynamics, based on the data of the storm available. The bias in $R_{2\%}$ calculation is equal to $0.056\,m$ with RMSE of $0.084\,m$. Higher swash levels in 1-d SWASH runs lead to overestimating the video measurements. Since poorly constrained model-parameter assumptions in the default configuration often lead to drawbacks in numerical models results, for the present work a sensitivity analysis of the Manning's friction coefficient on swash prediction, was conducted in the 1-d spatial domain. Results suggest that when the SWASH model is used for estimating real-world hazards, users should think carefully about choosing an appropriate roughness, by conducting sensitivity analysis and calibrating the model.

The reliability of the empirical formulations has been investigated, by comparing modelled with measured results. This study, although characterized by a database at a single field site, emphasized that the empirical models mostly overestimate the video-measurements as well as numerical predictions, probably due to the fact that most of the formulations do not properly take into account the complex hydrodynamic processes occurring during wave propagation. Conversely, by opportunely integrating information on the overall nearshore or surf zone slopes, the models of Mayer and Kriebel (1994) and Mather et al. (2011) are capable of better capturing the runup phenomena, with low errors. However, for engineering purposes, the definition of the runup and, consequently, of the potential flooded area on an embayed beach, the empirical formulations based on deep-water wave measurements give overestimated results, corresponding to a safe-side attitude.

Acknowledgement

This research is partially supported by Authority of Basin of Apulia Region (Italy), particularly in the persons of Prof. Antonio Di Santo (ex General secretary), Dott. Nicola Palumbo and Dott. Roberto Francioso. We thank our colleague Eng. Matteo Gianluca Molfetta who provided support in surveys management. Intervention co-financed by the Development Fund and Cohesion 2007-2013 - APQ search Apulia Region "Regional program in support of smart specialization and social and environmental sustainability - FutureInResearch"

References

Antuono, M., Soldini, L., Brocchini, M., 2012. On the role of the chezy frictional term near the shoreline. Theoretical and Computational Fluid Dynamics 26, 105–116.

Atkinson, A.L., Power, H.E., Moura, T., Hammond, T., Callaghan, D.P., Baldock, T.E., 2017. Assessment of runup predictions by empirical models on non-truncated beaches on the south-east australian coast. Coastal Engineering 119, 15 – 31.

Benson, M.A., Dalrymple, T., 1967. General field and office procedures for indirect discharge measurements. Technical Report. US Govt. Print. Off.,.

Birkemeier, W.A., 1985. Field data on seaward limit of profile change. Journal of Waterway, Port, Coastal, and Ocean Engineering 111, 598–602.

Blenkinsopp, C., Matias, A., Howe, D., Castelle, B., Marieu, V., Turner, I., 2016. Wave runup and overwash on a prototype-scale sand barrier. Coastal Engineering 113, 88 – 103. Barrier Dynamics Experiment II: sediment processes across a large-scale sand barrier.

Booij, N., Holthuijsen, L.H., Ris, R.C., 1996. The" SWAN" wave model for shallow water. Coastal Engineering Proceedings 1.

Bouvier, C., Balouin, Y., Castelle, B., 2017. Video monitoring of sandbar-shoreline response to an offshore submerged structure at a microtidal beach. Geomorphology 295, 297 – 305.

Brocchini, M., Baldock, T.E., 2008. Recent advances in modeling swash zone dynamics: Influence of surf-swash interaction on nearshore hydrodynamics and morphodynamics. Reviews of Geophysics 46. https://agupubs.onlinelibrary.wiley.com/doi/pdf/10.1029/2006RG000215.

Bruno, M., Molfetta, M., Petrillo, A., 2014. The influence of interannual variability of mean sea level in the adriatic sea on extreme values. Journal of Coastal Research , 241–246https://doi.org/10.2112/SI70-041.1.

Bruun, P., 1954. Coast erosion and the development of beach profiles. volume 44. US Beach Erosion Board.

Celli, D., Pasquali, D., De Girolamo, P., Di Risio, M., 2018. Effects of submerged berms on the stability of conventional rubble mound breakwaters. Coastal Engineering 136, 16–25.

Conde-Frias, M., Otero, L., Restrepo, J.C., Ortiz, J.C., Ruiz, J., Osorio, A.F., 2017. Swash oscillations in a microtidal dissipative beach. Journal of Coastal Research 33, 1408–1422.

De Roo, S., Suzuki, T., Kolokythos, G., Zhao, G., Verwaest, T., 2015. Numerical modelling of 2D wave transformation processes from nearshore to a shallow foreshore: comparison between the Mike21, swash and XBeach models, in: 36th IAHR World Congress, pp. 1–6.

Douglass, S.L., 1992. Estimating extreme values of run-up on beaches. Journal of Waterway, Port, Coastal, and Ocean Engineering 118, 220–224.

Elfrink, B., Baldock, T., 2002. Hydrodynamics and sediment transport in the swash zone: a review and perspectives. Coastal Engineering 45, 149–167.

Fonstad, M.A., Dietrich, J.T., Courville, B.C., Jensen, J.L., Carbonneau, P.E., 2013. Topographic structure from motion: a new development in photogrammetric measurement. Earth Surface Processes and Landforms 38, 421–430.

Gonçalves, J.A., Henriques, R., 2015. UAV photogrammetry for topographic monitoring of coastal areas. ISPRS Journal of Photogrammetry and Remote Sensing 104, 101–111.

Guimarães, P.V., Farina, L., Toldo, E., Diaz-Hernandez, G., Akhmatskaya, E., 2015. Numerical simulation of extreme wave runup during storm events in Tramandaí Beach, Rio Grande do Sul, Brazil. Coastal Engineering 95, 171–180.

Harwin, S., Lucieer, A., 2012. Assessing the accuracy of georeferenced point clouds produced via multi-view stereopsis from unmanned aerial vehicle (UAV) imagery. Remote Sensing 4, 1573–1599.

Henderson, S.M., Guza, R., Elgar, S., Herbers, T., Bowen, A., 2006. Nonlinear generation and loss of infragravity wave energy. Journal of Geophysical Research: Oceans 111.

Herbers, T.H.C., Elgar, S., Guza, R.T., 1994. Infragravity-frequency (0.005–0.05 hz) motions on the shelf. part i: Forced waves. Journal of Physical Oceanography 24, 917–927. https://doi.org/10.1175/1520-0485(1994)024<0917:IFHMOT>2.0.CO;2.

Holman, R.A., 1986. Extreme value statistics for wave run-up on a natural beach. Coastal Engineering 9, 527–544.

Holman, R.A., Stanley, J., 2007. The history and technical capabilities of Argus. Coastal Engineering 54, 477–491.

Hunt, I.A., 1959. Design of sea-walls and breakwaters. Transactions of the American Society of Civil Engineers 126, 542–570.

Lee, J., Park, J., Choi, J., 2013. Evaluation of sub-aerial topographic surveying techniques using total station and RTK-GPS for applications in macrotidal sand beach environment. Journal of Coastal Research .

Long, N., Millescamps, B., Guillot, B., Pouget, F., Bertin, X., 2016. Monitoring the Topography of a Dynamic Tidal Inlet Using UAV Imagery. Remote Sensing 8, 387.

Mancini, F., Dubbini, M., Gattelli, M., Stecchi, F., Fabbri, S., Gabbianelli, G., 2013. Using Unmanned Aerial Vehicles (UAV) for high-resolution reconstruction of topography: The structure from motion approach on coastal environments. Remote Sensing 5, 6880–6898.

Mase, H., 1989. Random wave runup height on gentle slope. Journal of Waterway, Port, Coastal, and Ocean Engineering 115, 649–661.

Mather, A.A., Stretch, D., Garland, G., 2011. WAVE RUN UP ON NATURAL BEACHES. Coastal Engineering Proceedings 1, 45.

Mayer, R.H., Kriebel, D.L., 1994. Wave runup on composite-slope and concave beaches. Coastal Engineering Proceedings 1.

Mentaschi, L., Besio, G., Cassola, F., Mazzino, A., 2015. Performance evaluation of Wavewatch III in the Mediterranean Sea. Ocean Modelling 90, 82–94.

Nielsen, P., Hanslow, D.J., 1991. Wave runup distributions on natural beaches. Journal of Coastal Research , 1139–1152.

Otsu, N., 1979. A threshold selection method from Gray-level. IEEE Transactions on Systems, Man, and Cybernetics SMC-9, 62–66.

Reis, A.H., Gama, C., 2010. Sand size versus beachface slope – An explanation based on the Constructal Law. Geomorphology 114, 276–283.

Ruggiero, P., Komar, P.D., McDougal, W.G., Marra, J.J., Beach, R.A., 2001. Wave runup, extreme water levels and the erosion of properties backing beaches. Journal of Coastal Research , 407–419.

Salmon, S.A., Bryan, K.R., Coco, G., 2007. The use of video systems to measure run-up on beaches. Journal of Coastal Research 50, 211–215.

Sancho, A., Guillén, J., Simarro, G., Medina, R., Cánovas, V., 2012. Beach inundation prediction during storms using different wave heights as inputs. Coastal Engineering Proceedings 1, 32.

Saponieri, A., Damiani, L., 2015. Numerical analysis of infiltration in a drained beach. International Journal of Sustainable Development and Planning 10, 467–486.

Smit, P., Janssen, T., Holthuijsen, L., Smith, J., 2014. Non-hydrostatic modeling of surf zone wave dynamics. Coastal Engineering 83, 36–48.

Soldini, L., Antuono, M., Brocchini, M., 2012. Numerical modeling of the influence of the beach profile on wave run-up. Journal of Waterway, Port, Coastal, and Ocean Engineering 139, 61–71.

Stockdon, H.F., Holman, R.A., Howd, P.A., Sallenger Jr, A.H., 2006. Empirical parameterization of setup, swash, and runup. Coastal Engineering 53, 573–588.

Stockdon, H.F., Thompson, D.M., Plant, N.G., Long, J.W., 2014. Evaluation of wave runup predictions from numerical and parametric models. Coastal Engineering 92, 1–11.

Suzuki, T., Verwaest, T., Hassan, W., Veale, W., Reyns, J., Trouw, K., Troch, P., Zijlema, M., 2011. The applicability of swash model for wave transformation and wave overtopping: a case study for the flemish coast, in: Proc. 5th Int. Conf. Advanced Computational Methods Engineering (ACOMEN 2011), Liège, Belgium, pp. 14–17.

Svendsen, I.A., 2006. Introduction to nearshore hydrodynamics. volume 24. World Scientific.

Thévenaz, P., Sage, D., Unser, M., 2012. Bi-exponential edge-preserving smoother. IEEE Transactions on Image Processing 21, 3924–3936.

Thorndike Saville, J., 1957. Wave run-up on composite slopes. Coastal Engineering Proceedings 1, 41.

Tuan, T.Q., Oumeraci, H., 2010. A numerical model of wave overtopping on seadikes. Coastal Engineering 57, 757–772.

Turner, I.L., Harley, M.D., Drummond, C.D., 2016. Uavs for coastal surveying. Coastal Engineering 114, 19 – 24.

Valentini, N., Damiani, L., Molfetta, M.G., Saponieri, A., 2017a. New coastal video-monitoring system achievement and development. Coastal Engineering Proceedings 1, 11.

Valentini, N., Saponieri, A., Damiani, L., 2017b. A new video monitoring system in support of coastal zone management at apulia region, italy. Ocean & Coastal Management 142, 122–135.

Valentini, N., Saponieri, A., Molfetta, M.G., Damiani, L., 2017c. New algorithms for shoreline monitoring from coastal video systems. Earth Science Informatics 10, 495–506.

Vousdoukas, M., Kirupakaramoorthy, T., Oumeraci, H., De La Torre, M., Wübbold, F., Wagner, B., Schimmels, S., 2014. The role of combined laser scanning and video techniques in monitoring wave-by-wave swash zone processes. Coastal Engineering 83, 150–165.

Vousdoukas, M.I., Velegrakis, A.F., Dimou, K., Zervakis, V., Conley, D.C., 2009. Wave run-up observations in microtidal, sediment-starved pocket beaches of the Eastern Mediterranean. Journal of Marine Systems 78, S37–S47.

Vousdoukas, M.I., Wziatek, D., Almeida, L.P., 2012. Coastal vulnerability assessment based on video wave run-up observations at a mesotidal, steep-sloped beach. Ocean Dynamics 62, 123–137.

Westoby, M., Brasington, J., Glasser, N., Hambrey, M., Reynolds, J., 2012. Structure-from-motion photogrammetry: A low-cost, effective tool for geoscience applications. Geomorphology 179, 300–314.

Zijlema, M., Stelling, G., 2008. Efficient computation of surf zone waves using the nonlinear shallow water equations with non-hydrostatic pressure. Coastal Engineering 55, 780–790.

Zijlema, M., Stelling, G., Smit, P., 2011. SWASH: An operational public domain code for simulating wave fields and rapidly varied flows in coastal waters. Coastal Engineering 58, 992–1012.